

## INFLUENCE OF SIZE AND NUMBER OF NACA 0012 BLADES ON THE MECHANICAL POWER OF WIND TURBINE-POWERED CAR

Moktar A. Hashem Mohamad<sup>1</sup>

Youssef Kassem<sup>2</sup>

Mechanical Engineering Department, Higher Institute for Sciences and Technology, Tobruk, Libya (Email: [wiseness2014@gmail.com](mailto:wiseness2014@gmail.com))<sup>1</sup>

Near East University, Faculty of Engineering, Mechanical Engineering Department, Nicosia, 99138, North Cyprus (Email: [yousseuf.kassem@neu.edu.tr](mailto:yousseuf.kassem@neu.edu.tr))<sup>2</sup>

### ABSTRACT

The vertical axis wind turbine (VAWT) can harness wind energy. However, there are still significant gaps in our understanding of VAWT aerodynamics and performance, particularly when it comes to designing and selecting blade chords and height. In the case of a wind car, it utilizes a vertical axis and employs a varying number of NACA 0012 blades positioned at a  $2^\circ$  angle of attack and mounted at different angles. These blades are directly connected to wheels using various mechanisms, while gears are used to convert wind energy into mechanical energy to overcome the load on the main shaft during low speeds. The objective of this study is to investigate the influence of blade number and size on the mechanical power of the rotor. Specifically, we measured the torque and mechanical power acting on a blade at an airflow speed of 4 m/s and an angular velocity of 13.056 rad/s, based on previous scientific research.

**Key Words:** Aerofoil Blades, energy, torque, mechanical power, wind car

### 1. INTRODUCTION

As the global reserves of fossil fuels steadily decrease, there is a growing global interest in utilizing renewable energy sources for power generation. Conventional energy sources have faced criticism due to their detrimental effects, such as air pollution and significant greenhouse gas emissions, which have resulted in a decline in public perception. Furthermore, the impending depletion of fossil fuels like oil, coal, and natural gas shortly catalyzes for researchers to intensify their investigations into alternative energy resources. Thus, renewable energy technologies like wind power, offer numerous advantages. They have the advantage of producing no greenhouse gas emissions and causing minimal environmental impact when compared to conventional methods of energy production [1, 3]. Wind energy is considered an alternative solution to mitigate air pollution and reduce reliance on fossil fuel consumption [4, 5]. It has several advantages such as that harnessing wind power is viable in various locations worldwide and commercial wind turbines have the capability to generate a substantial amount of energy, their efficient design and technology allow for the production of significant power outputs, contributing to meeting energy demands on a various scale. The wind turbine is a device to convert wind energy into mechanical power [4, 5].

Generally, wind power is commonly used to generate electricity; it is not typically used as a direct source of propulsion for cars [6]. Most cars on the road today are powered by internal combustion engines, electric motors, or a combination of both [7]. However, there have been some experimental projects and concepts that explore the idea of using wind power to propel vehicles. One such concept is the "Land Sail" or "Wind-powered car." These vehicles are designed with a large sail or set of sails attached to the body, harnessing the force of the wind to generate forward motion. The sail can be adjusted to catch the wind at various angles and positions, allowing the vehicle to move in different directions. It's important to note that wind-

powered cars have limitations and are not as practical or efficient as conventional vehicles. They heavily rely on the availability and strength of the wind, making them unsuitable for most urban or non-windy environments. Wind direction changes, gusts, and the need for open spaces with adequate wind flow are also significant challenges for wind-powered cars. Additionally, wind-powered cars face difficulties with control and safety. Steering and braking can be challenging, especially in strong winds, and there is a risk of instability or tipping over. Consequently, wind-powered cars are not commonly used for everyday transportation and are primarily seen as recreational vehicles or experimental prototypes [8].

In the literature, numerous studies and prototypes have been developed to explore the concept of wind-powered cars. For instance, the Greenbird is a wind-powered vehicle specifically designed to break land speed records. It was created by engineer Richard Jenkins and set the world land speed record for wind-powered vehicles in 2009. The Greenbird achieved an average speed of 126.2 mph (202.9 km/h) across the windswept surface of Ivanpah Dry Lake in Nevada, USA [9]. The Ventomobile is a wind-powered vehicle developed by students at the Technical University of Delft in the Netherlands. It features a lightweight design and a large turbine mounted at the front, which captures wind energy to propel the vehicle forward. The Ventomobile participated in the World Solar Challenge, an international solar car race, in the "Cruiser Class" category, which allows for both solar and wind power [10]. Moreover, Blackbird Wind-powered Car was created by the Wind Explorer team in 2010, the Blackbird is a lightweight, aerodynamic car designed to be powered by wind and a small electric motor [11]. It gained attention for its successful journey across Australia, covering approximately 3,000 kilometers (1,864 miles) using only wind power and a minimal amount of battery assistance [11]. Additionally, the Nemesis is a wind-powered electric car developed by Ecotricity, a UK-based renewable energy company [12]. It was built to showcase the potential of wind power and electric vehicles. The Nemesis set a new UK land speed record for electric vehicles in 2010, reaching a top speed of 151 mph (244 km/h) [12]. Besides, several scientific studies have estimated the drag, lift forces, and mechanical power of wind-powered cars using various shapes of the blades [13-16]. Çamur and Kassem [13] determined the characteristics of drag and the torque of three C-section blade wind cars with various blades geometric. The results showed that the C-section blades demonstrated the highest torque output at a diameter of 0.6m. Çamur and Kassem [14] analyzed the torque, lift, and drag forces exerted by various NACA airfoil shapes, which could potentially be employed in generating electric power or propelling the wind-powered car. Kassem [16] utilized computational fluid dynamics (CFD) through Autodesk CFD to analyze the aerodynamic behavior of three different models of a vertical-axis wind turbine car. The results demonstrated that the larger single C-section blade exhibited the highest efficiency for the vertical axis wind turbine car. This was attributed to its ability to generate the maximum drag force when compared to the other blade designs.

Based on the above, the objective of this study is to explore the impact of the number of blades and blade geometries (blade chord and blade height) on the mechanical power generated by a wind-powered car equipped with a three-bladed NACA 0012 aerofoil at an angle of attack of  $2^\circ$ . The velocity analysis approach was employed for this investigation. The wind speed and angular velocity used in the analysis were set at 4 m/s and 13 rad/s, respectively, based on previous scientific studies. Microsoft Excel was utilized to present and analyze the data related to mechanical power.

## 2. AEROFOIL THEORY

Airplane wings, propeller blades, windmill blades, compressor and turbine blades in a jet engine, and hydrofoils all share a common feature known as an airfoil. An airfoil refers to the specific shape of an object that is strategically positioned in the path of an airstream to generate aerodynamic forces.

The NACA airfoil shape is commonly utilized for aircraft wings. Developed between 1929 and 1947 under the supervision of Eastman Jacobs at the NACA's Langley Field Laboratory, NACA airfoils are characterized by several key parameters. These parameters typically include maximum thickness, maximum camber, the position of maximum thickness, position of maximum camber, and nose radius [18]. In general, when a horizontal wing is intersected by a vertical plane that runs parallel to the centerline, the resulting section typically exhibits a shape similar to the one depicted in Figure 1 [19]. This section is commonly referred to as an airfoil.

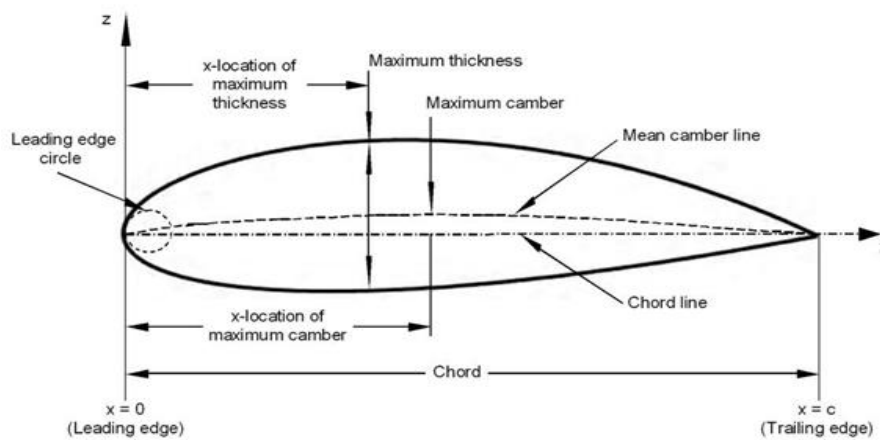


**Figure 1:** Airfoil-section geometry and its nomenclature [19]

The airfoil shape, as depicted in Figure 1, can be expressed analytically based on various design parameters. Geometric factors play a crucial role in determining the aerodynamic characteristics of an airfoil section. These factors include (1) the leading-edge radius, (2) the mean camber line, (3) the maximum thickness and thickness distribution of the profile, and (4) the trailing-edge angle. An airfoil is specifically designed to be placed within an airstream to generate an aerodynamic force, as illustrated in Figure 2 [20]. The resulting lift and drag forces depend on the airfoil's shape, the angle of attack, and the viscosity of the air.

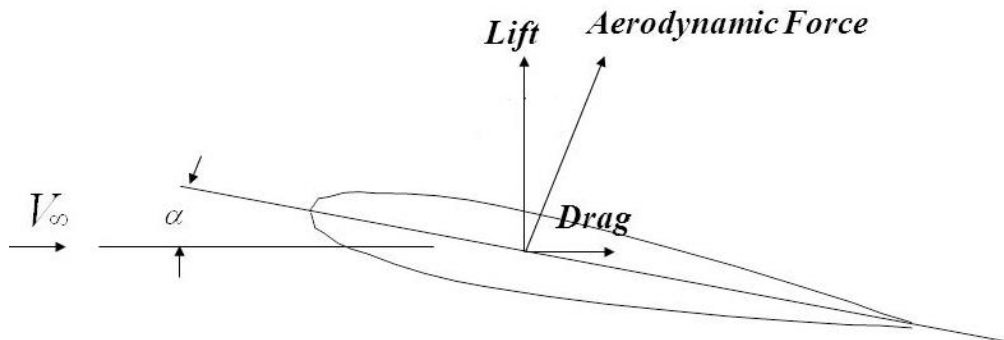


**Figure 2:** Aerodynamic forces

To simplify the analysis, these forces are often described using lift and drag coefficients, which are single variables in the respective equations. However, due to the complexities involved, the determination of these

coefficients typically relies on experimental or numerical studies. Therefore, the equations for lift ( $F_L$ ) and drag ( $F_D$ ) can be represented as [6]:

$$F_L = \frac{1}{2} V_\infty^2 \rho C_L A$$

$$F_D = \frac{1}{2} V_\infty^2 \rho C_D A$$

where  $\rho$  represents the density of air,  $V_\infty$  denotes the relative velocity of the airflow,  $A$  corresponds to the area of the airfoil as viewed from above,  $C_L$  and  $C_D$  represent the lift and drag coefficient, respectively. Eq. (3) shows the relationship between drag and lift coefficient [21]

$$C_D = C_{D,0} + \frac{C_L^2}{\pi ar} \quad , \quad ar = \frac{b^2}{A_p} \quad (3)$$

where, the drag coefficient at zero lift is represented as  $C_{D,0}$ . The aspect ratio is denoted as  $ar$ , while  $b$  refers to the wingspan or the distance from one wingtip to the other wingtip of the airplane. Additionally,  $A_p$  represents the planform area.

During the flight of an airfoil, the pressure and velocity on its surface are non-uniform. Figure 3 illustrates typical pressure distributions for a specific section at different angles of incidence. To facilitate the analysis of non-dimensional pressure differences, a reference point is necessary. In this case, the pressure far upstream, denoted as  $P_\infty$ , serves as the reference datum. To quantify the pressure variations, the coefficient of pressure ( $C_p$ ) is introduced.

$$C_p = \frac{P - P_\infty}{\frac{1}{2} \rho V_\infty^2}$$

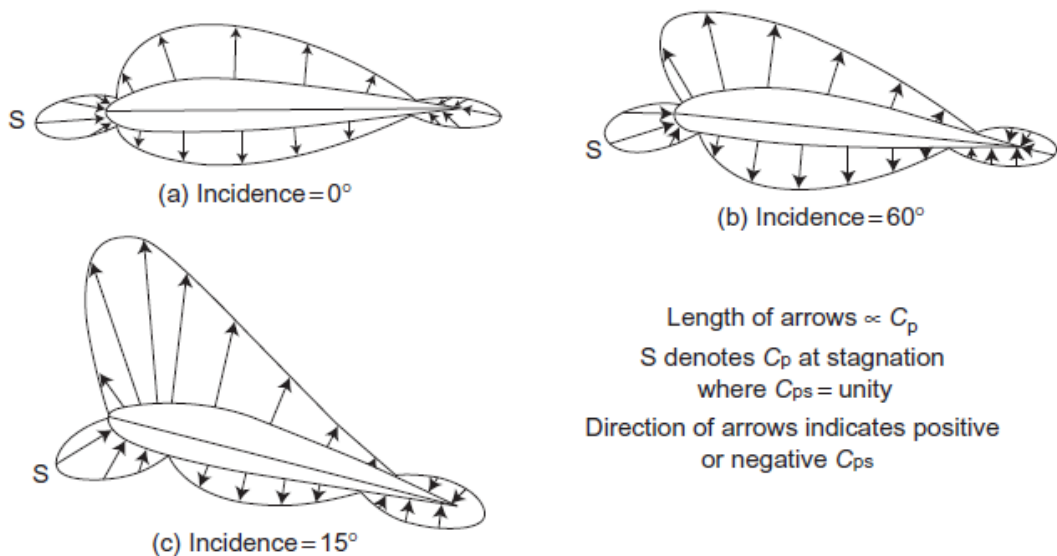


**Figure 3:** Typical pressure distributions on an airfoil section

Consider Figure 4, which represents an aerofoil positioned at an angle of incidence  $\alpha$  relative to a fluid flow moving from left to right at a velocity ( $V_\infty$ ). The axes  $O_x$  and  $O_z$  are aligned parallel and perpendicular to the chord line, respectively.

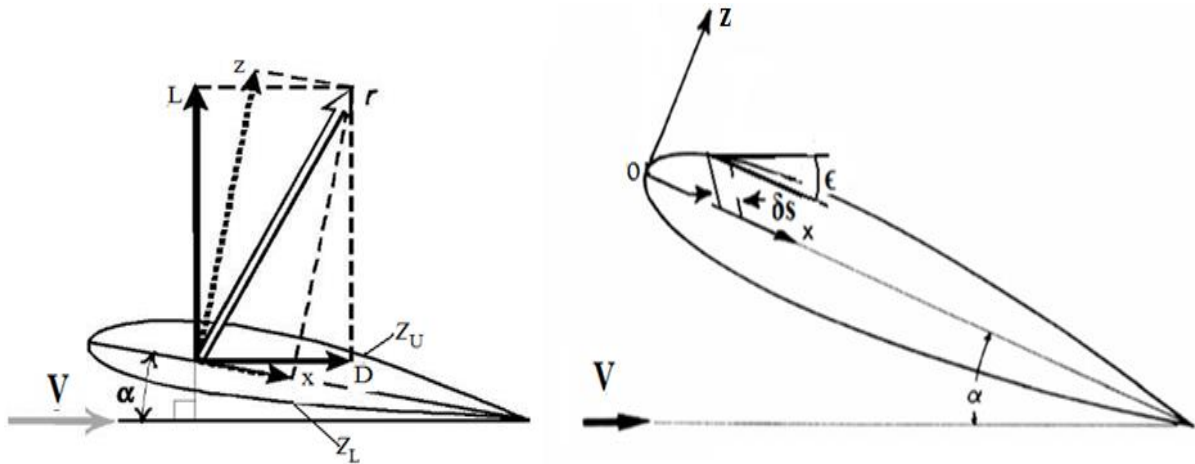


**Figure 4:** Normal pressure force on an element of the airfoil surface

If we consider a small element of the upper surface of the aerofoil with length ( $\delta s$ ), the inward force acting perpendicular to the surface can be represented as  $P_u \delta s$ . This force can be further divided into components  $\delta x$  and  $\delta z$  in the  $x$  and  $z$  directions, respectively.

$$\begin{aligned} \delta Z_u &= -P_u \cos \epsilon \\ &= -P_u \delta s \cos \epsilon \\ &= -\delta x \end{aligned}$$

per unit span

Similarly, for the lower surface

$$\begin{aligned} \delta Z_l &= -P_l \delta s \end{aligned}$$

per unit span

We now add these two contributions and integrate them for  $x$  between  $x = 0$  and  $x = c$  to get

$$\begin{aligned} Z &= - \int_0^c P_u dx \\ &+ \int_0^c P_l dx \end{aligned} \tag{9}$$

But we can always subtract a constant pressure from both  $P_u$  and  $P_l$  without altering the value of  $Z$ , so, we can write

$$\begin{aligned} Z &= - \int_0^c (P_u - P_\infty) dx \\ &+ \int_0^c (P_l - P_\infty) dx \end{aligned} \tag{10}$$

Where  $P_\infty$  is the pressure in the free stream (we could equally well use any other constant pressure, e.g. the stagnation pressure in the free stream). Eq. (10) can readily be converted into coefficient form. Recalling that the aerofoil section is of unit span, the area  $A = 1 \times c = c$  so,

$$C_Z = \frac{Z}{\frac{1}{2}\rho V_\infty^2 c} = \frac{1}{\frac{1}{2}\rho V_\infty^2 c} \left[ - \int_0^c (P_u - P_\infty) dx + \int_0^c (P_l - P_\infty) dx \right] \quad (11)$$

Remembering that  $(l/c) dx = d(x/c)$  and that the definition of pressure coefficient is

$$C_p = \frac{P - P_\infty}{\frac{1}{2}\rho V_\infty^2 c}$$

We see that

$$C_Z = - \int_0^1 (P_u - P_l) d\left(\frac{x}{c}\right) \quad (13)$$

Similar arguments lead to the following relations for X.

$$\delta X_u = P_u \delta s \sin \epsilon \quad \delta X_l = P_l \delta s \sin \epsilon \quad \delta s \sin \epsilon = \delta z \quad (14)$$

Giving

$$C_X = \oint_c C_p d\left(\frac{z}{c}\right) = \int_{Z_{ml}}^{Z_{mu}} \Delta C_p d\left(\frac{z}{c}\right) \quad (15)$$

Where  $Z_{mu}$  and  $Z_{ml}$  are respectively the maximum and minimum values of  $z$ , and  $\Delta C_p$ , is the difference between the values of  $C_p$  acting on the fore and rear points of an aerofoil for a fixed value of  $z$ . Aerodynamic coefficients of Airfoil can be obtained from Eqs. (16) and (17)

$$C_L = C_Z \cos \alpha - C_X \sin \alpha \quad (16)$$

$$C_D = C_Z \sin \alpha + C_X \cos \alpha \quad (17)$$

Moreover, the work by Houghto & Carpenter [22] describes the NACA four-digit series, along with the equations for constructing these series. These equations specifically outline the thickness distribution and camber lines associated with the four-digit series of NACA airfoils. The profile of four-digit wing sections of airfoils is defined by the following parameters:

- a). The first digit represents the maximum camber of the airfoil, expressed as a percentage of the chord length.

- b). The second digit indicates the distance of the maximum camber point from the leading edge of the airfoil, given in tens of percent of the chord length.
- c). The last two digits specify the maximum thickness of the airfoil, represented as a percentage of the chord length.

The formula for the shape of a symmetrical airfoil, specifically the NACA four-digit series represented by "00XX," where "XX" is replaced by the percentage of thickness to chord, can be expressed as follows:

$$z = \frac{t/c}{0.2} c \left[ a \sqrt{\frac{x}{c}} - b \left(\frac{x}{c}\right) - c \left(\frac{x}{c}\right)^2 + d \left(\frac{x}{c}\right)^3 - e \left(\frac{x}{c}\right)^4 \right] \quad (18)$$

where  $c$  is the chord length,  $x$  is the position along the chord from 0 to  $c$ ,  $z$  is the half thickness at a given value of  $x$ ,  $t/c$  is the relative thickness (thickness ratio) and  $a$ ,  $b$ ,  $c$ ,  $d$ , and  $e$  are constants (Table 1).

Now the coordinates  $(x_u, z_u)$  of the upper airfoil surface and  $(x_L, z_L)$  of the lower airfoil surface are:

$$z_u = +z \quad \text{and} \quad z_L = -z \quad \text{for} \quad x_u = x_L = x \quad (19)$$

**Table 1** Constants of a four-digit symmetrical airfoil

a	b	c	d	e
0.2969	0.1260	0.3516	0.2843	0.1015

The formula used to calculate the mean camber line for an un-symmetric NACA 4-digit is

$$z = \begin{cases} h \frac{x}{x_h^2} \left( 2x_h - \frac{x}{c} \right), & \text{from } x = 0 \text{ to } x = x_h c \\ h \frac{c - x}{(1 - x_h)^2} \left( 1 + \frac{x}{c} - 2x_h \right), & \text{from } x = x_h c \text{ to } x = c \end{cases} \quad (20)$$

where  $h$  is the maximum camber,  $x_h$  is the location of the maximum camber,  $c$  is the chord length and  $x$  is the position along the chord from 0 to  $c$ .

The calculation of velocity distribution and aerodynamic coefficients has been conducted using the singularity method in the previous section. However, for convenience, these parameters can also be evaluated using numerical summation formulas. The specific details of these calculations are described in the work of F. Riegels and E. Truckenbrodt [23]. This reference provides further information and guidance on the numerical methods employed for the evaluation of these parameters. For the numerical quadrature the coordinates of the profile at the  $N$ -discrete nodes are determined as;

$$X_m = \frac{1}{2} \left( 1 + \cos \frac{\pi m}{N} \right), \quad m = 0, 1, \dots, N \quad (21)$$

The velocity distribution on the profile contour at discrete points  $X_n$  is obtained through the following summation formula;

$$\frac{V_k(X_n)}{U_\infty} = \frac{1}{X_n^*} \left[ a_n + 2 \sum_{m=1}^{N-1} A_{nm} Z_m^t \pm 2 \sum_{m=1}^{N-1} C_{nm} Z_m^s \pm \alpha \left( b_n + 2 \sum_{m=1}^{N-1} H_{nm} Z_m^t \right) \right] \quad (22^1)$$

Where

$$X_n^* = \sqrt{C_n + \left(\frac{dZ^t}{d\phi}\right)_n^2} \quad (23^1)$$

and an ,bn , cn, Anm, Cnm, and Hnm are Fourier series coefficients, and N is the number of discrete nodes. The pressure coefficient distribution on the profile contour is obtained through the following summation formula;

$$\begin{aligned} C_p &= 1 \\ &- V_k^2(X_n) \end{aligned}$$

The aerodynamic coefficients are obtained through Eqs. (23) and (24)

$$\begin{aligned} C_L &= C_Z \cos\alpha \\ &- C_X \sin\alpha \end{aligned} \quad (25)$$

$$\begin{aligned} C_D &= C_Z \sin\alpha \\ &+ C_X \cos\alpha \end{aligned} \quad (26)$$

where

$$\begin{aligned} C_Z &= \left[ \sum_{I=1}^{\infty} \left( \frac{C_{p_i} + C_{p_{i+1}}}{2} \right) \left| \frac{x_i}{c} - \frac{x_{i+1}}{c} \right| \right]_{\text{upper}} \\ &- \left[ \sum_{I=1}^{\infty} \left( \frac{C_{p_i} + C_{p_{i+1}}}{2} \right) \left| \frac{x_i}{c} - \frac{x_{i+1}}{c} \right| \right]_{\text{lower}} \end{aligned} \quad (27)$$

$$\begin{aligned} C_X &= \left[ \sum_{I=1}^{\infty} \left( \frac{C_{p_i} + C_{p_{i+1}}}{2} \right) \left| \frac{x_i}{c} - \frac{x_{i+1}}{c} \right| \right]_{\text{FRONT}} \\ &- \left[ \sum_{I=1}^{\infty} \left( \frac{C_{p_i} + C_{p_{i+1}}}{2} \right) \left| \frac{x_i}{c} - \frac{x_{i+1}}{c} \right| \right]_{\text{AFT}} \end{aligned} \quad (28)$$

### 3. WIND TURBINE

The classification of wind turbines is based on two significant criteria: aerodynamic force and design. Wind turbines can be categorized as either drag-based or lift-based, depending on their aerodynamic performance. Drag-based turbines, also known as low-speed turbines, utilize the drag force of the wind to generate power. On the other hand, some turbines are designed to harness the lift force as well, and these are recognized as high-speed rotors. Lift-based turbines can capture a higher amount of wind power compared to their drag-based counterparts, making them the more prevalent solution in modern wind energy applications.

Wind turbines are further classified into two main types: horizontal axis wind turbines (HAWTs) and vertical axis wind turbines (VAWTs). HAWTs are currently the most widely used commercial wind turbines. The blades of HAWTs rotate parallel to the direction of the wind. They offer advantages such as high turbine efficiency, high power density, low cut-in wind speeds, and relatively low cost per unit power

<sup>1</sup> Coefficients  $a_n, b_n, c_n, A_{nm}, C_{nm}, H_{nm}$  required to calculate the velocity distribution on the contour profile using Eq. (22) and Eq. (23) for  $N = 12$ , can be found in reference [23].

output. In contrast, VAWTs have blades that rotate perpendicular to the ground. One of the advantages of VAWTs is their ability to accept wind from any direction, eliminating the need for yaw control mechanisms. The VAWT is an omnidirectional wind turbine that can accept wind from all directions without the need for a yawing mechanism, as mentioned in reference [24]. Moreover, VAWTs are generally expected to produce less noise compared to HAWTs. It features straight blades attached to the drive shaft via support arms. The main advantage of this concept is its simplicity. The wind turbine consists of only a few parts and has only one rotating component. By eliminating the gearbox, yawing system, and pitch system, maintenance requirements are reduced [25]. The blades of the H-rotor are fixed and cannot be rotated out of the wind. Power absorption is controlled by an electrical control system combined with passive stall control. The blade design allows for stalling, limiting power absorption at high wind speeds. In VAWTs, the generator is located at the bottom of the tower, simplifying installation and maintenance. Since the nacelle is absent, the tower can be lighter, reducing structural loads and erection difficulties [25]. The generator design focuses on efficiency, cost-effectiveness, and minimizing maintenance, with less emphasis on the generator's physical size. Additionally, locating the control system at ground level provides convenient access [25].

In the design of a vertical axis wind turbine (VAWT) with two, three, or four blades, the blades are arranged symmetrically around a vertical axis. The angles of the blades are carefully optimized to operate based on the lift principle. As the VAWT rotates, the blades experience two forces: their rotational speed and the incoming wind speed. These speeds are combined vectorially, resulting in a total apparent wind speed with a specific angle of attack, as illustrated in Figure 5.

The incoming air stream, which is parallel to the blades, creates regions of high and low pressure on the blade surfaces, leading to the generation of lift and drag forces. The resultant oblique lift force applies a torque on the shaft to which the blades are connected, causing them to rotate in the same direction as the motion of the blades. This rotation generates an overall positive torque, which can be harnessed as electrical power through the use of a generator.

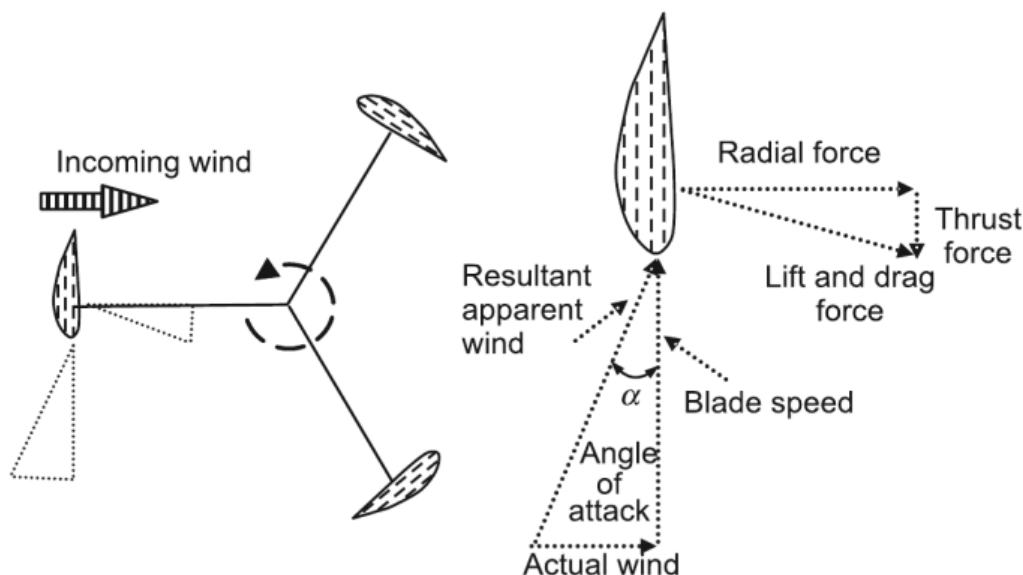


**Figure 5:** Lift principle of three-bladed VAWT Rotor

However, a major limitation of VAWTs is their inability to self-start due to the symmetric blade configuration. Therefore, a starting mechanism is necessary. The electrical generator is typically operated as a motor initially to accelerate the VAWT until the wind passes over the blade aerofoils, generating lift

forces. Once the VAWT reaches a sufficient speed, it transitions into the generating mode. The torque produced by the VAWT is a consequence of the changes in the apparent wind direction relative to the moving blades [26].

To summarize, VAWTs rely on the lift principle for generating torque. They require an initial starting procedure due to the symmetric blade design, after which they can harness the wind's power to generate electricity.

#### 4. MECHANICAL POWER

A wind turbine is composed of two main components: the rotor and the generator. The rotor is responsible for capturing the energy from the wind. It consists of blades that are designed to efficiently convert the kinetic energy of the wind into rotational energy. As the wind blows, it imparts a force on the blades, causing them to rotate. This rotation generates torque, which is a measure of the twisting or turning force applied to the rotor shaft. The generated torque is then transferred to the generator. In most wind turbines, this is achieved through a gearbox, which increases the rotational speed of the rotor to a level suitable for the generator. The generator, typically an electrical generator, receives the mechanical energy from the rotor shaft and converts it into electrical energy. This conversion is achieved by electromagnetic induction, where the rotating motion of the shaft within the generator creates a magnetic field that induces an electrical current in the generator's coils.

The power required to maintain the motion of an object with a constant velocity can be defined as the product of the force (F) acting on the object and the velocity (V) at which it is moving. Mathematically, the power (P) can be expressed as:

$$P = F \times V$$

The power is measured in units of watts (W) in the International System of Units (SI). It represents the rate at which work is done or energy is transferred. In the context of the object moving along a straight path with constant velocity, the power indicates the amount of energy that needs to be supplied to the object to counteract any resistance or frictional forces and maintain its motion at the same speed.

Furthermore, for a shaft that rotates with a constant angular speed under the effect of torque, the power can be defined as the product of the torque (T) and the angular velocity ( $\omega$ ). Mathematically, the power (P) can be expressed as:

$$P = T \times \omega$$

#### 5. PROTOTYPE

In this study, a wind car with varying numbers of NACA airfoil blades is investigated, and it is directly connected to the chassis through different links and gears. The wind car incorporates a vertical wind turbine mounted on the chassis. Figure 6 illustrates the shape of the wind car with three airfoil blades, serving as an example. The turbine captures the wind, leading to the generation of a pressure drag force, which in turn causes the turbine to rotate around its fixed axis. The geometric dimensions of the wind turbine used in the wind car are provided in Table 2.

**Table 2.** Geometrical dimension of the wind turbine of wind car

Type of Airfoil	NACA 0012
Attack angle [°]	2
Blade number [-]	2, 3, 4, 5, 6
Blade chord [cm]	30, 40, 60, 80, 100
Rotor diameter [m]	1
Blade height [m]	1, 1.25, 1.5, 2, 2.25, 2.5, 2.75, 3

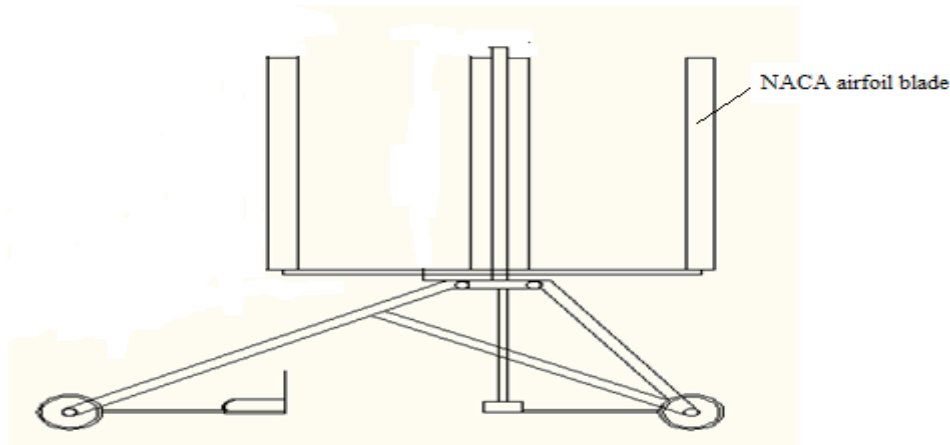


**Figure 6:** Shape of the wind car with three aerofoil blades

In Figure 7, a visual representation is provided to demonstrate several key elements of the VAWT system. These elements include:

1. Free stream velocity ( $U_\infty$ ): This refers to the speed of the incoming wind, which is depicted in the figure.
2. The direction of the speed of the blades ( $\omega R$ ): The figure indicates the direction in which the blades rotate around the vertical axis. This rotational speed is denoted by  $\omega R$ .
3. Position of the blade with angle  $\gamma$ : The figure illustrates the specific orientation of a blade, represented by the angle  $\gamma$ . This angle indicates the position of the blade relative to the incoming wind.
4. The direction of rotation of the blades for the NACA blade: The figure indicates the overall rotation direction of the blades. This information is relevant specifically to the NACA blade design being depicted.

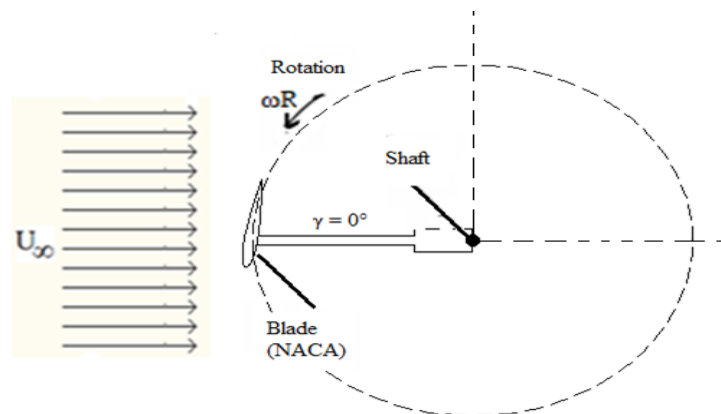


**Figure 7:** Schematic diagram of one blade rotor for a single NACA airfoil blade

During the rotation of the VAWT, the free stream velocity  $U_\infty$  can be broken down into two components. The first component aligns with the direction of velocity and is utilized to determine the skin friction drag force. This component contributes to the drag experienced by the blades as they interact with the moving air. The second component is perpendicular to the velocity direction and is responsible for calculating the pressure drag force. This component arises from the pressure differences between the upper and lower surfaces of the NACA airfoil.

As the speed of the blades ( $\omega R$ ) impacts both surfaces of the NACA airfoil, and considering the influence of the free stream velocity on the upper or lower surface, which depends on the profile's location, the free stream velocity is either added to or subtracted from the speed of the blades. This adjustment depends on the direction of the velocity, as depicted in Figure 8.

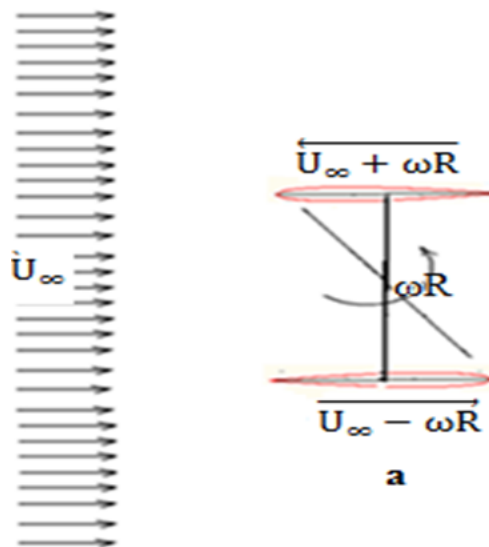


**Figure 8:** Direction of free stream velocity and speed of the blades during the rotations

The diagram presented in Figure 9 illustrates the analysis of forces acting on a single blade of the NACA airfoil. The blade is divided into four distinct regions based on angular position:

- a). The first region spans from  $0^\circ$  to  $90^\circ$ .
- b). The second region covers the range of  $90^\circ$  to  $180^\circ$ .
- c). The third region encompasses angles between  $180^\circ$  and  $270^\circ$ .
- d). The fourth region extends from  $270^\circ$  to  $360^\circ$ .

These divisions allow for a detailed examination of the forces experienced by the blade throughout a complete rotation cycle. By studying the forces in each specific region, a comprehensive understanding of the blade's performance and aerodynamic characteristics can be obtained.

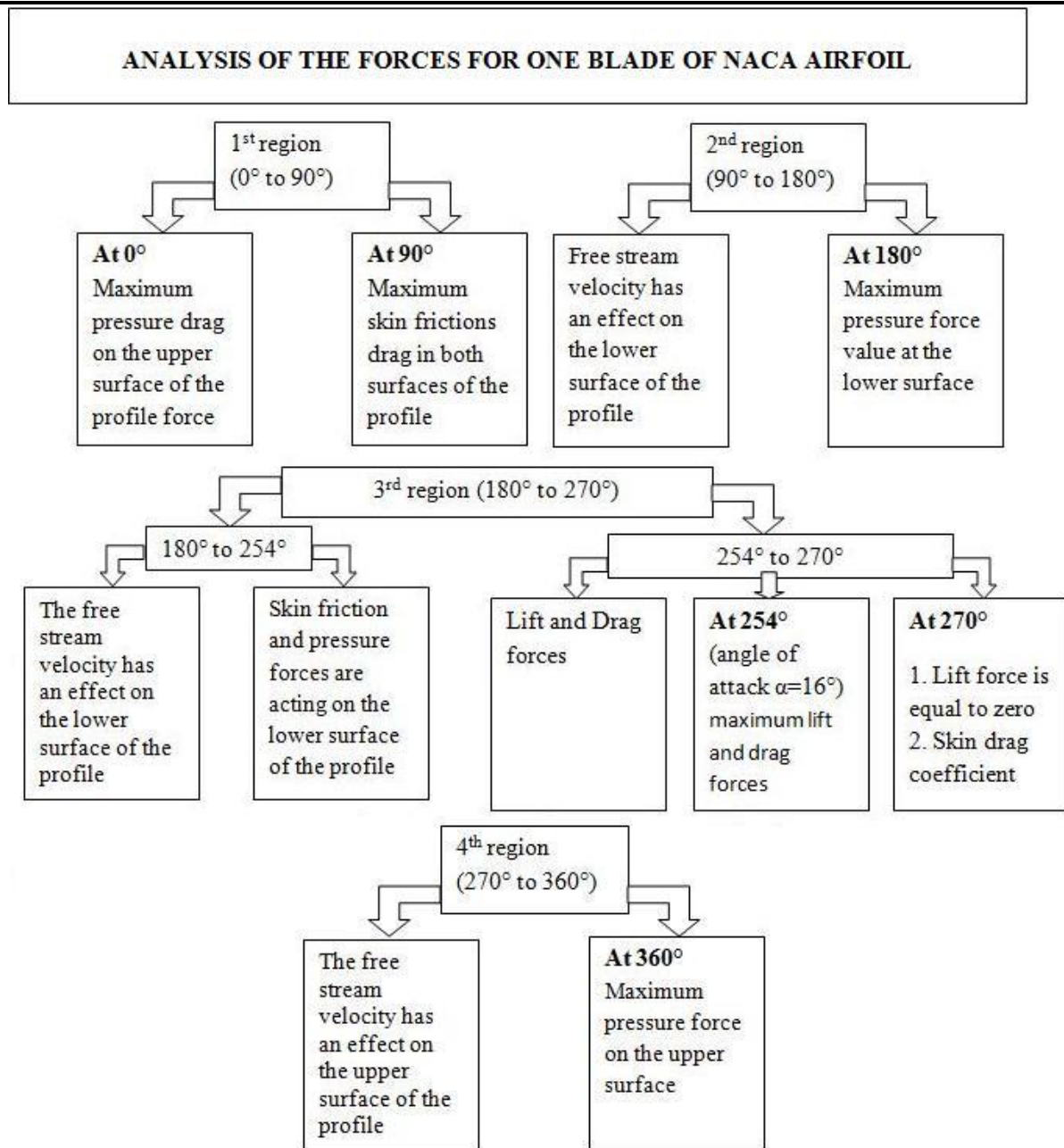


**Figure 9:** Analysis of the forces for one blade

## 5. RESULTS AND DISCUSSION

Figure 10 displays flow charts outlining the step-by-step procedure for calculating the forces and torque of a vertical wind turbine utilizing the NACA airfoil. These flow charts provide a systematic guide to computing the various parameters involved in assessing the performance and mechanical characteristics of the turbine. By following the outlined steps, one can determine the forces exerted on the blades and calculate the resulting torque generated by the turbine. These flow charts serve as a useful tool in the analysis and design of vertical wind turbines utilizing NACA airfoils.

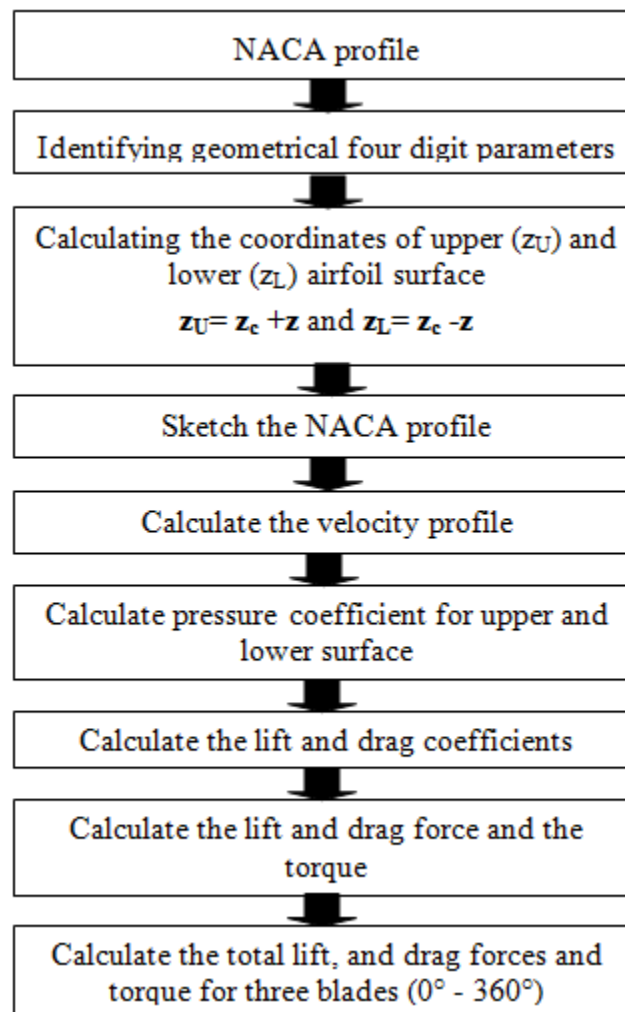


**Figure 10:** Identification of the procedure to compute the drag force and torque of vertical wind turbine

By utilizing the flow chart specific to the NACA profile, it becomes possible to calculate the aerodynamic force and coefficients for an individual blade. Moreover, the same flow chart can be employed to calculate the total forces and torque for any given number of blades.

In the context of a wind turbine-powered car, the torque, and mechanical power were computed for different numbers of NACA 0012 blades set at a  $2^\circ$  angle of attack. Figures 11 and 12 depict the variations in torque and mechanical power as the rotor angle ( $\gamma$ ) changes for these varying numbers of blades. Additionally, calculations were performed at  $2^\circ$  intervals between  $0^\circ$  to  $360^\circ$ , with a blade height of 2 meters and a blade chord of 30 cm.

Observing Figures 7 and 8, it is evident that the torque and mechanical power increase with the number of blades. The periodic nature of the graphs for the two, three, four, five, and six-blade configurations of the NACA 0012 profile is visible, with the motion repeating itself in a consistent pattern.

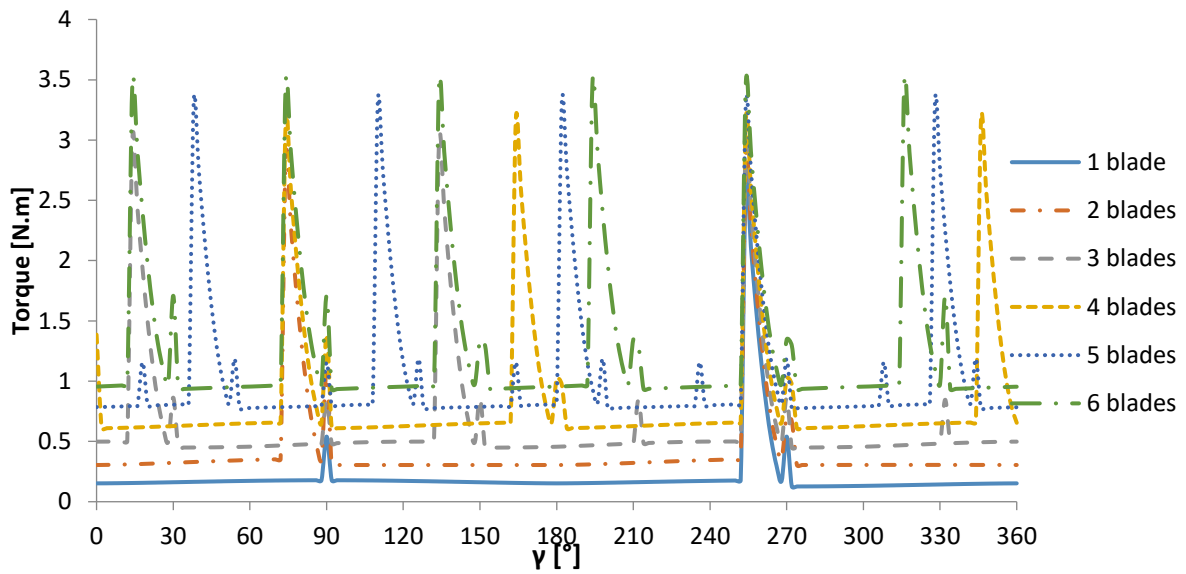


**Figure 11:** Torque versus Angle of Rotation ( $\gamma$ )

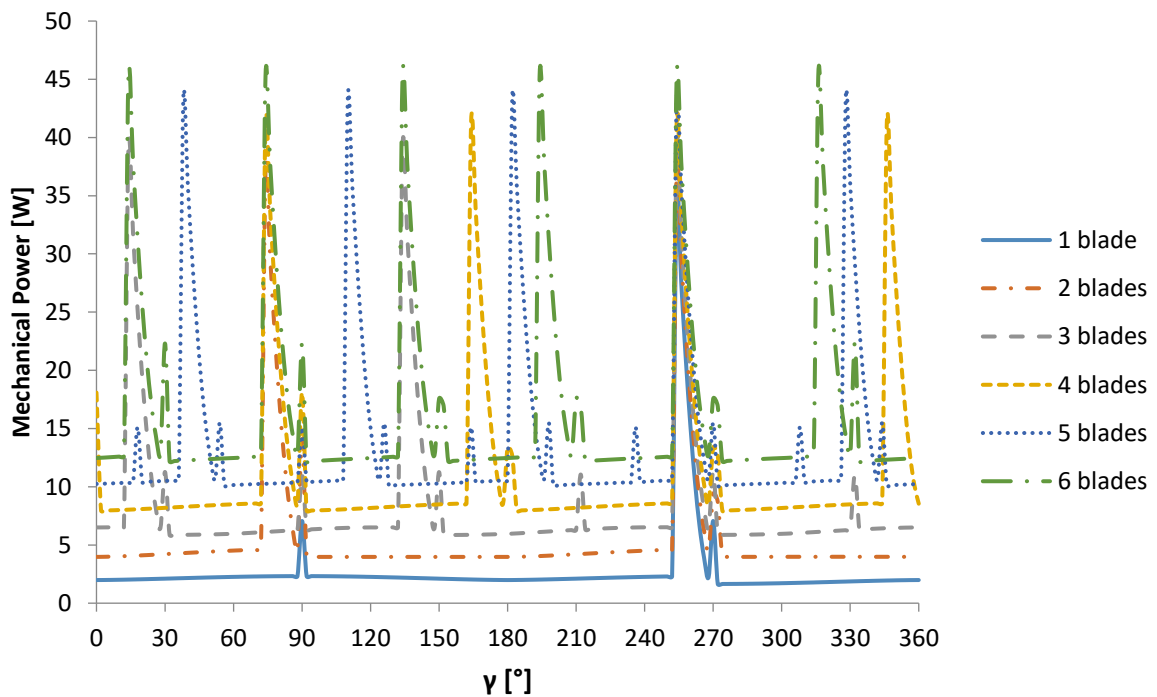


**Figure 12:** Mechanical power versus Angle of Rotation ( $\gamma$ )

Table 3 presents a comprehensive compilation of the mechanical power values generated by varying numbers of NACA 0012 blades while maintaining a consistent size of 2 meters blade height and 30 cm blade chord. Figure 13 provides a visual representation of the average mechanical power produced by different numbers of NACA 0012 blades, all under the same wind speed. Notably, the graph illustrates a significant and rapid increase in mechanical power as the number of blades is increased. This observation highlights the positive correlation between the number of blades and the amount of mechanical power generated.

**Table 3.** Average mechanical power for a variable number of NACA 0012 blades (30 cm blade chord and 2 m blade height)

Number of blades	Average mechanical power [W]
1	2.71
2	5.42
3	8.12
4	10.83
5	13.54
6	16.25

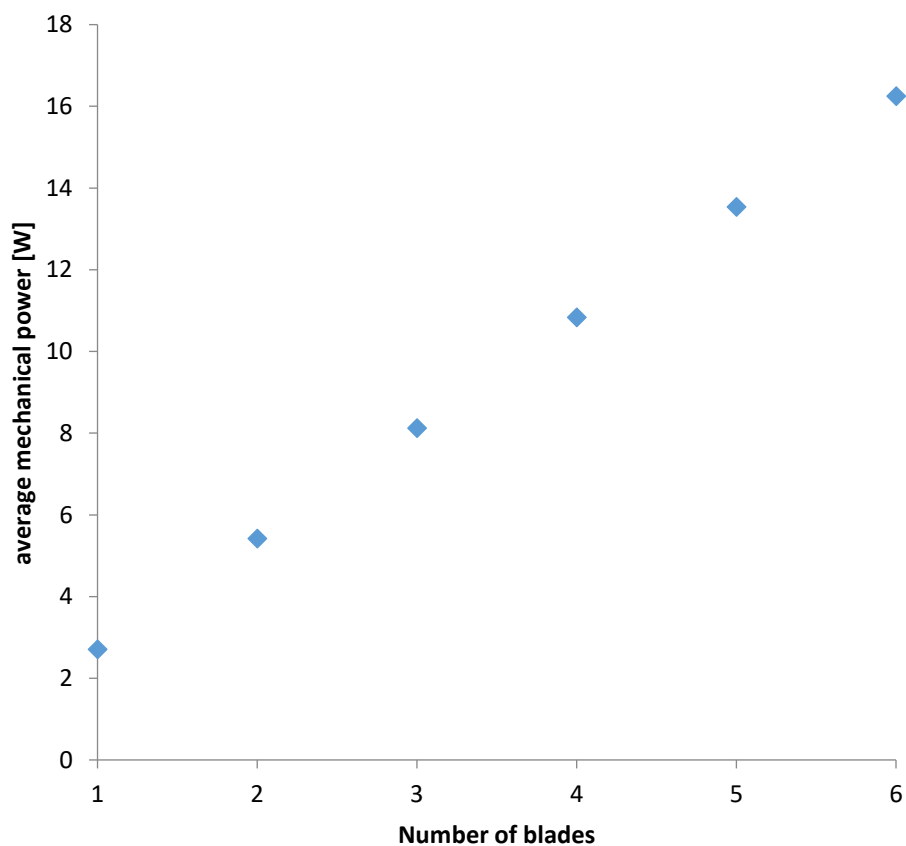


**Figure 13:** Average mechanical power for a variable number of NACA 0012 blades (30 cm blade chord and 2 m blade height)

Figures 14 and 15 depict the relationship between the average mechanical power and two key parameters: blade chord and blade height. These figures consider varying numbers of wind turbine blades. Analyzing Figures 13, 14, and 15 together, it becomes evident that increasing the number of blades, blade height, and blade chord leads to a higher production of mechanical power by the wind turbine-powered car. Furthermore, the figures demonstrate a clear linear trend, indicating that as the size and number of blades increase, the average mechanical power consistently follows suit.

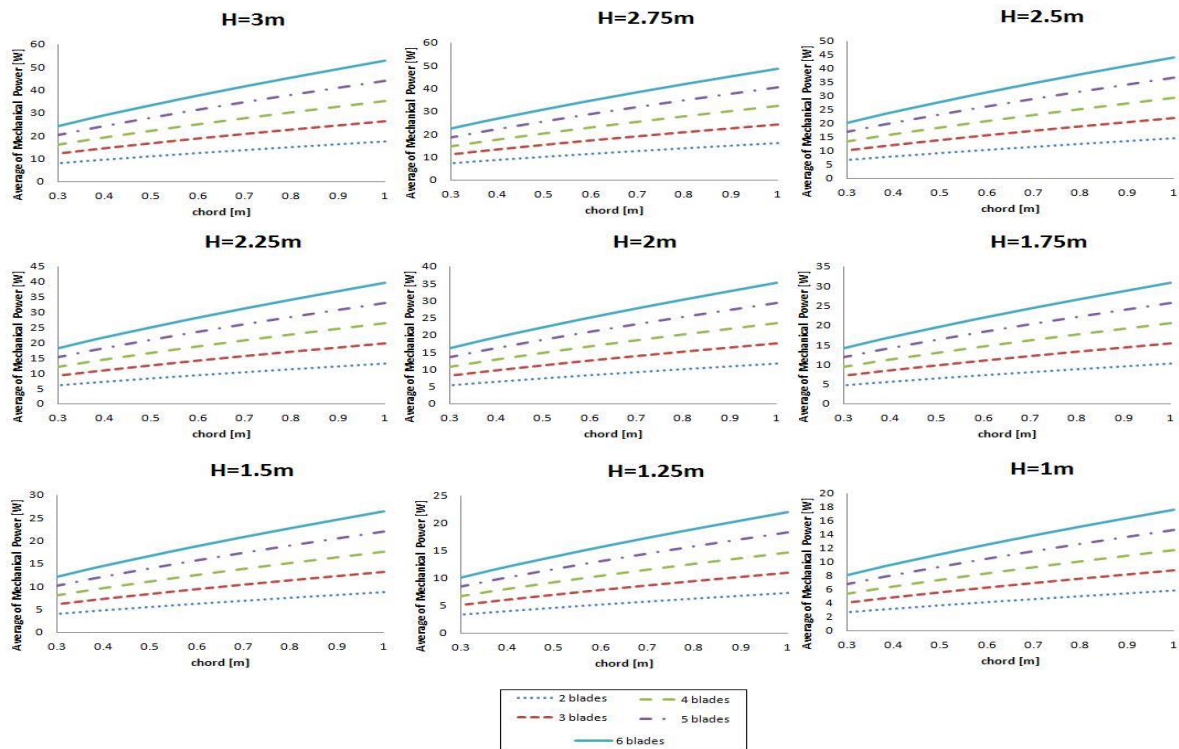


**Figure 14:** Average mechanical power of variable number blades versus blade chord for different blade height

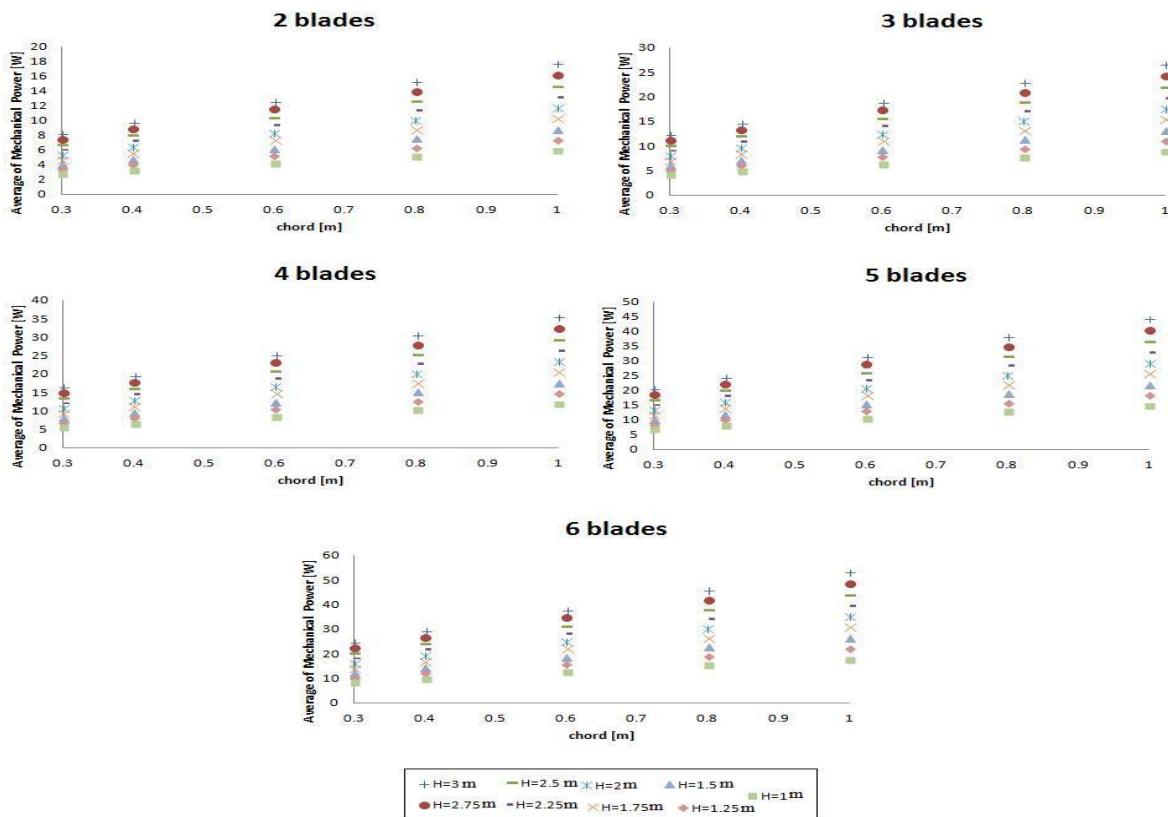


**Figure 15:** Average mechanical power of the different heights of blade wind turbine versus blade chord for a variable number of blades

## 5. CONCLUSIONS

The conclusions drawn from this study can be summarized as follows:

- The primary objective of this research was to investigate the relationship between the number of blades, their size, and the mechanical power generated by a wind turbine-powered car at a wind speed of 4 m/s and a 2° angle of attack.
- The influence of blade chords, blade height, and varying numbers of blades on the aerodynamics and performance of vertical axis wind turbines were thoroughly examined.
- Mechanical power and torque calculations were performed for different numbers of blades and sizes of wind turbine-powered cars. The results were then compared to identify trends and patterns.
- The comparison and analysis of mechanical power and torque revealed that both are significantly influenced by the size and number of blades employed in the wind turbine system.
- The results indicate that increasing the size and number of NACA 0012 blades leads to higher mechanical power production by the wind turbine-powered car, even when considering the same wind speed and angle of attack.
- It was observed that the performance of the vertical wind turbine improved as the number of blades, blade chord, and blade height increased.

## REFERENCES

1. Flanzamaton, C. M., Gökçekuş, H., & Kassem, Y. Renewable Energy Can Help to Reduce Climate Change in Nigeria: Evidence from Previous Studies.
2. Çamur, H., Kassem, Y., & Alessi, E. (2021). A techno-economic comparative study of a grid-connected residential rooftop PV panel: the case study of Nahr El-Bared, Lebanon. *Engineering, Technology & Applied Science Research*, 11(2), 6956-6964.
3. Gokcekus, H., Kassem, Y., Mason, M. N., & Selay, J. M. (2023). Hundred percent renewable wastewater treatment plant: techno-economic assessment using a ret screen, case study Syria. *Future Technology*, 2(1), 46-57.
4. Kassem, Y., Gökçekuş, H., & Janbein, W. (2021). Predictive model and assessment of the potential for wind and solar power in Rayak region, Lebanon. *Modeling Earth Systems and Environment*, 7, 1475-1502.
5. Kassem, Y., Gokcekus, H., Camur, H., & Abdelnaby, A. H. A. (2022). Wind Power Generation Scenarios in Lebanon. *Engineering, Technology & Applied Science Research*, 12(6), 9551-9559.
6. Kassem, Y. (2011). Determination of the aerodynamic parameters of the airfoils for a wind car (master dissertation, Near East University).
7. Momoh, O. D., & Omoigui, M. O. (2009, September). An overview of hybrid electric vehicle technology. In 2009 IEEE vehicle power and propulsion conference (pp. 1286-1292). Ieee.
8. Nieuwenhuis, P. (2014). *Sustainable automobility: understanding the car as a natural system*. Edward Elgar Publishing.
9. The Guardian. (2009). Jorge Chapa writes on Greenbird, the world's fastest wind-powered vehicle. The Guardian. <https://www.theguardian.com/environment/2009/apr/01/greenbird-wind-powered-vehicle>
10. ScienceDaily. (2008a, August 6). Wind-powered vehicle, Ventomobile, ready to race in the Netherlands. ScienceDaily. <https://www.sciencedaily.com/releases/2008/08/080804123039.htm>
11. Stewart, J. (2022, February 24). Blackbird Wind-powered car sails against the storm. BBC Future. <https://www.bbc.com/future/article/20120727-the-wind-beneath-my-wheels>

12. George, A. (2012, September 25). A Windmill manufacturer builds an EV coupe that looks suspiciously familiar. Wired. <https://www.wired.com/2012/09/electricity-lotus-exige/>
13. Çamur, H., & Kassem, Y. (2013). Creating the wind energy for operating the 3-C-section blades wind car. In *Advanced Materials Research* (Vol. 622, pp. 1188-1193). Trans Tech Publications Ltd.
14. Çamur, H., & Kassem, Y. (2013). Operating a three-blade-wind car with wind energy. In *Advanced Materials Research* (Vol. 622, pp. 1199-1203). Trans Tech Publications Ltd.
15. Kassem, Y., & Çamur, H. Wind Power Vehicle Uses 3 Double C-Section Blades. *Engineering Sciences International Research Journal*, 1(1).
16. Kassem, Y., & Hüseyin, Ç. (2015). Wind turbine-powered car uses 3 single big C-section blades. In *International Conference on Aeronautical & Manufacturing Engineering (ICAAME 2015)* (pp. 42-45).
17. Kassem, Y. (2018). Computational study on vertical axis wind turbine car: static study. *Modeling Earth Systems and Environment*, 4, 1041-1057.
18. Kassem, Y., Çamur, H., & Alhuoti, S. M. A. (2019). MATLAB Simulator can support student learning for Fluid Mechanics courses in the Mechanical Engineering Department. *methods*, 2, 6.
19. Phillips, W. F. (2004). *Mechanics of flight*. John Wiley & Sons.
20. Chen, J., & Wang, Q. (Eds.). (2017). *Wind turbine airfoils and blades: Optimization design theory* (Vol. 3). Walter de Gruyter GmbH & Co KG.
21. Janna, W. S. (2020). *Introduction to fluid mechanics*. CRC press.
22. Houghton, E. L., & Carpenter, P. W. (2003). *Aerodynamics for engineering students*. Elsevier.
23. Schlichting, H. and Truckenbrodt, E. (1979). *Aerodynamics of the Airplane*, United state of America
24. Kassem, Y., Çamur, H., Bahroun, A. A., Abughnida, O. A., & Alghazali, A. (2018). Performance investigation of Savonius Turbine with New Blade Shape: Experimental and Numerical study. *International Journal of Applied Engineering Research*, 13(10), 8546-8560.
25. Eriksson, S., Bernhoff, H., & Leijon, M. (2008). Evaluation of different turbine concepts for wind power. *renewable and sustainable energy reviews*, 12(5), 1419-1434.
26. Abzug, M. J., & Larrabee, E. E. (2002). *Airplane stability and control: a history of the technologies that made aviation possible* (Vol. 14). Cambridge University Press.